# $Eu^{3+}$-Doped $In_2O_3$ Nanophosphors: Electronic Structure and Optical Characterization

**Qingbo Xiao, Yongsheng Liu, Liqin Liu, Renfu Li, Wenqin Luo, and Xueyuan Chen***

*Key Laboratory of Optoelectronic Materials Chemistry and Physics, Fujian Institute of Research on the Structure of Matter, Chinese Academy of Sciences, Fuzhou, Fujian 350002, China*

*Received: March 23, 2010; Revised Manuscript Received: April 8, 2010*

Rare-earth ion-doped semiconducting nanocrystals have attracted extensive attention due to the ability to tailor their optical properties via size control and to achieve efficient luminescence through the host sensitization. A new type of nanophosphor based on $Eu^{3+}$-ion-doped $In_2O_3$ nanocrystals, synthesized via a facile solvothermal method, shows intense and well-resolved intra4f emissions of $Eu^{3+}$ upon bandgap excitation. Optical properties of $Eu^{3+}$ occupying two crystallographic sites ($C_2$ and $S_6$) are systematically investigated by means of high-resolution emission and excitation spectra at 10−300 K. The crystal-field (CF) analysis and Judd−Ofelt (JO) intensity calculation of $Eu^{3+}$ at $C_2$ site yield relatively large CF strength and JO intensity parameters, indicating the good optical performance of this nanophosphor. Due to a small filling factor (0.43) of the $In_2O_3$ nanocrystals, the radiative lifetime of $^5D_0$ of $Eu^{3+}$ is found to be significantly affected by the surrounding media with various refractive indices, which is about 3 times longer than that in the submicrometer counterparts. Furthermore, as compared to the submicrometer counterparts, an enhanced host-to-$Eu^{3+}$ energy transfer with higher quenching temperature is observed due to more effective photon-induced carrier localization and trapping around $Eu^{3+}$ in nanocrystals.

## 1. Introduction

Recently, rare-earth (RE)-doped nanocrystals and nanocomposites have gained much research interest due to their unique optical properties and potential applications in many technical fields.[1–7] Indium sesquioxide ($In_2O_3$) is a wide bandgap semiconductor (direct bandgap energy of ∼2.9−3.2 eV[8–10]) and a good candidate as a host material for RE ions because of its good mechanical, optical, and thermal properties. $In_2O_3$ has a large exciton Bohr radius of 2.14 nm,[11] thus optical properties of RE ions incorporated in very small $In_2O_3$ nanocrystals are expected to be modified due to quantum confinement effects. It is also anticipated that RE luminescence can be efficiently sensitized by exciton recombination in $In_2O_3$ nanocrystals. Optical properties of $In_2O_3$:$RE^{3+}$ microstructures[12,13] and nanopowders[14–16] have been reported recently. Kim et al.[13] and Choi et al.[16] observed $Er^{3+}$ emission around 1.54 $\mu$m in $In_2O_3$:$Er^{3+}$ under direct excitation of $Er^{3+}$ ions. The $Eu^{3+}$ luminescence was observed in $In_2O_3$:$Eu^{3+}$ quantum dots (QDs)[15] upon indirect excitation above 350 nm at room temperature, due possibly to the host sensitization. However, the above luminescence lines of $Eu^{3+}$ were broad (full width at half-maximum (fwhm) of ∼9 nm for the 614-nm peak) and weak, indicating that the $Eu^{3+}$ ions were probably located at the surface (or near the surface) of $In_2O_3$ nanocrystals. Antic-Fidancev et al.[12] observed the resolved emission lines of $Eu^{3+}$ in $In_2O_3$ polycrystalline powders in the 1990s, but the emission spectra presented were weak, and only 21 levels of the low-lying $^7F_J$ ($J$ = 0, 1, 2, 3, 4) multiplets were identified. So far, no spectroscopic evidence for the incorporation of $Eu^{3+}$ into $In_2O_3$ nanocrystals has been presented. A detailed study of optical spectroscopy of $Eu^{3+}$ incorporated into lattice sites of $In_2O_3$ nanocrystals, such as luminescence dynamics, crystal-field (CF) analysis and Judd−Ofelt (JO) intensity calculation, is still lacking. A comprehensive investigation of the optical spectroscopy and luminescence dynamics may gain more insight into optical behaviors of RE ions in semiconducting nanocrystals.

In this paper, $Eu^{3+}$ ion-doped $In_2O_3$ nanocrystals emerging as a new type of semiconducting nanophosphor were synthesized via a simple solvothermal method. High-resolution emission and excitation spectra of $Eu^{3+}$ in $In_2O_3$ nanocrystals were measured, and the CF levels were determined. The energy level fitting, JO intensity parameters, and luminescence lifetimes were investigated in detail. Furthermore, host-to-$Eu^{3+}$ energy transfer (ET) was demonstrated, and a possible ET mechanism was proposed.

## 2. Experimental Section

**Nanoparticle Synthesis.** $Eu^{3+}$-doped $In_2O_3$ nanophosphors were prepared by a solvothermal method similar to the procedure reported by Xu et al.[17] Typically, a mixture of 0.5 mmol $In(NO_3)_3 \cdot 6(H_2O)$ and $Eu(CH_3COO)_3 \cdot 3(H_2O)$ with a nominal molar ratio of Eu/In 3.0 at.% was dissolved in 25 mL ethanol, and then 6 mL oleic acid was added dropwise under vigorous stirring to afford the transparent solution. The precursor solution was transferred into a 40 mL Teflon-lined autoclave and maintained at 180 °C for 24 h. After being cooled to room temperature naturally, the brown precipitates were collected and washed with ethanol several times, dried at 60 °C for 12 h, and finally annealed at 400, 600, 800, and 1000 °C for 2 h, respectively, to yield the final products. For comparison, pure $In_2O_3$ nanocrystals were prepared using the same procedure followed by annealing at 600 °C for 2 h.

**Characterization.** The chemical compositions of the final products were measured by induction-coupled plasma (ICP) analysis (Ultima2, Jobin Yvon). Powder X-ray diffraction (XRD) patterns were collected using a PANalytical X'Pert PRO powder diffractometer with Cu Kα1 radiation ($\lambda$ = 0.154 nm). The morphology of the samples was characterized by a JEOL-2010 transmission electron microscope (TEM). Ultraviolet/

* To whom correspondence should be addressed. E-mail: xchen@fjirsm.ac.cn.

10.1021/jp102592q 
Published on Web 05/04/2010

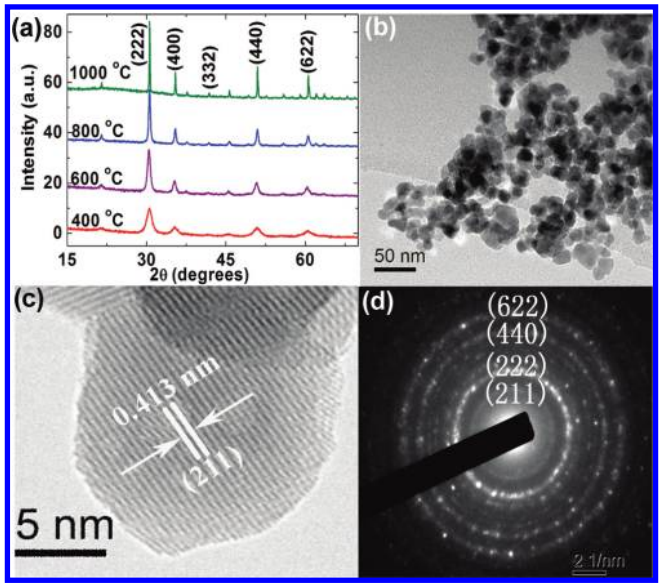


**Figure 1.** (a) XRD patterns of $In_2O_3$:$Eu^{3+}$ nanocrystals annealed at different temperatures. (b) TEM image, (c) high-resolution TEM image, and (d) SAED pattern of $In_2O_3$:$Eu^{3+}$ nanocrystals annealed at 600 °C.

visible (UV/vis) diffuse reflectance spectra were measured by Perkin-Elmer Lambda 900 UV/vis/NIR Spectrometer using $BaSO_4$ as a blank. Emission and excitation spectra and transient decays were recorded on an Edinburgh Instruments FLS920 spectrofluorimeter equipped with both continuous (450 W) and pulsed xenon lamps. For low temperature measurements, samples were mounted on a closed-cycle cryostat (10−350 K, DE202, Advanced Research Systems). For site-selective spectroscopy, the excitation (or emission) monochromator's slits were set as small as possible to maximize the instrumental resolution. The best wavelength resolution is 0.05 nm. The line intensities and positions of the measured spectra were calibrated according to the FLS920 correction curve and standard mercury lamp.

## 3. Results and Discussion

**3.1. Crystal Structure and Morphology Characterization.** The concentration of $Eu^{3+}$ was determined to be 2.3 at % by an ICP emission spectrometer. Figure 1a shows the XRD patterns for $In_2O_3$:$Eu^{3+}$ nanoparticles annealed at different temperatures. These XRD diffraction peaks for all the samples can be exclusively indexed as cubic bixbyite $In_2O_3$ (JCPDS card No. 71-2194), indicating the presence of highly crystalline $In_2O_3$:$Eu^{3+}$ nanocrystals without any other impurity phases such as $Eu_2O_3$. By means of the Debye−Scherrer equation, the average sizes of the $In_2O_3$:$Eu^{3+}$ nanoparticles annealed at 400, 600, 800, and 1000 °C are estimated to be 14, 21, 48, and 110 nm, respectively. The particle size of $In_2O_3$:$Eu^{3+}$ nanoparticles heated at 600 °C decreases slightly compared to that of pure $In_2O_3$ counterparts (∼28 nm), which reveals that the incorporation of $Eu^{3+}$ into $In_2O_3$ nanocrystals might restrain the nanocrystal growth to some extent. Hereafter, the $In_2O_3$:$Eu^{3+}$ (2.3 at %) samples annealed at 600 and 1000 °C will be referred to as the nanocrystals and the submicrometer counterparts of $In_2O_3$:$Eu^{3+}$, respectively.

The morphology of $In_2O_3$:$Eu^{3+}$ nanocrystals was characterized by TEM. As shown in Figure 1b, the TEM image shows that the $In_2O_3$:$Eu^{3+}$ nanocrystals are irregular spheres with the diameters ranging from 15 to 20 nm. The corresponding high-resolution TEM image (Figure 1c) clearly demonstrates the high crystallinity of $In_2O_3$:$Eu^{3+}$ nanocrystals. Lattice fringes are very clear with an observed *d*-spacing of 0.413 nm, which is in good agreement with the lattice spacing for the (211) plane of cubic $In_2O_3$. The selected area electron diffraction (SAED) pattern also reveals the polycrystalline nature of $In_2O_3$:$Eu^{3+}$ nanocrystals, and the diffraction rings in Figure 1d can be well indexed as (211), (222), (440), and (622) planes of cubic $In_2O_3$.

**3.2. Emission and Excitation Spectra.** According to the crystal structure of $In_2O_3$, two distinct sites are expected for RE ions in the In lattice, namely, a low symmetry site of $C_2$ and a centrosymmetric site of $S_6$. As shown in Figure 2a, upon direct excitation from the ground state $^7F_0$ to $^5D_2$ of $Eu^{3+}(C_2)$ at 465.1 nm, sharp and abundant emission lines of $Eu^{3+}$ in $In_2O_3$ nanocrystals centered at 533.0, 580.4, 586.3, 611.0, 648.4, 709.4, 741.4, and 804.4 nm are observed at 10 K, which correspond to $^5D_1 \rightarrow {}^7F_1$ and $^5D_0 \rightarrow {}^7F_J$ ($J = 0, 1, 2, 3, 4, 5, 6$) transitions of $Eu^{3+}(C_2)$, respectively. The fwhm of the peak at 611.0 nm is ca. 0.78 nm, an order of magnitude narrower than that of the 614-nm peak in QDs.[15] These emission lines of $Eu^{3+}$ in $In_2O_3$ nanocrystals are totally different from that of $Eu_2O_3$[18] polycrystalline powders in terms of line positions and shapes, suggesting that $Eu^{3+}$ ions are incorporated in the $In_2O_3$ nanocrystals instead of the formation of $Eu_2O_3$ clusters. Figure 2b shows the excitation spectrum of $In_2O_3$:$Eu^{3+}$ nanocrystals at 10 K. By monitoring the strongest emission peak of the forced electric dipole (ED) transition $^5D_0 \rightarrow {}^7F_2$ of $Eu^{3+}$ at 611.0 nm, sharp excitation peaks centered at 467.4, 528.2, and 580.4 nm are observed, which are attributed to the direct excitation of $Eu^{3+}$ from the ground state $^7F_0$ to different $^5D_J$ ($J = 2, 1, 0$) multiplets, respectively. More interestingly, besides the direct excitation lines of $Eu^{3+}$, an intense broad UV band centered at 350 nm that originates from the bandgap of $In_2O_3$ nanocrystals is also presented in Figure 2b, indicating that the $Eu^{3+}$ emissions can be achieved via an efficient nonradiative ET process from the $In_2O_3$ host to $Eu^{3+}$. Similar broad excitation bands centered at 364 nm are also observed in submicrometer counterparts (Figure S1 in the Supporting Information). The peaks of excitation bands are close to the bandgap values determined from UV/vis reflectance spectra (350 and 378 nm for $In_2O_3$:$Eu^{3+}$ nanocrystals and submicrometer counterparts, respectively, Figure S2). Because of the overlap between the conduction band of $In_2O_3$ nanocrystals and higher excited states of $Eu^{3+}$, no excitation lines from $^5L_6$ or $^5D_3$ multiples of $Eu^{3+}$ were detected in the excitation spectrum at 10 K. By contrast, weak $^7F_0 \rightarrow {}^5L_6$ excitation lines of $Eu^{3+}$ can be observed as the broad UV band becomes quenched above 200 K (inset of Figure 2b). On the basis of the high-resolution emission and excitation spectra at 10 and 250 K, 48 CF levels below 25500 $cm^{-1}$ of $Eu^{3+}$ at the $C_2$ site of $In_2O_3$ have been located and assigned in Table 1, which agree well with the partial levels assigned by Antic-Fidancev et al.[12] Note that the energy levels of $^5L_6$, $^5D_{1,2}$, and $^7F_{5,6}$ of $Eu^{3+}$ in $In_2O_3$ nanoparticles were not reported previously.

For $Eu^{3+}$ ions at $S_6$ site, only magnetic dipole (MD) induced transitions are allowed, which obey the selection rule $\Delta J = 0, \pm 1$ (except $J = 0 \rightarrow 0$). As assigned in Figure 3a, two emission lines corresponding to $^5D_0 \rightarrow {}^7F_1$ transition of $Eu^{3+}(S_6)$ were observed upon bandgap excitation of $In_2O_3$:$Eu^{3+}$ nanocrystals at 10 K. The CF splitting of $^7F_1$ for the $S_6$ site is determined to be 271 $cm^{-1}$. The peak at 593.8 nm is unusually strong due to coincident overlap with the $Eu^{3+}(C_2)$ emissions, as compared to the direct excitation of $^7F_0 \rightarrow {}^5D_2$ of $Eu^{3+}(C_2)$ at 465.1 nm (Figure 3b). The intense $Eu^{3+}$ emissions upon bandgap excitation further verify an efficient host-to-$Eu^{3+}$ ET. By monitoring the $^5D_0 \rightarrow {}^7F_1$ transition of $Eu^{3+}(S_6)$ at 584.4 nm, two distinct

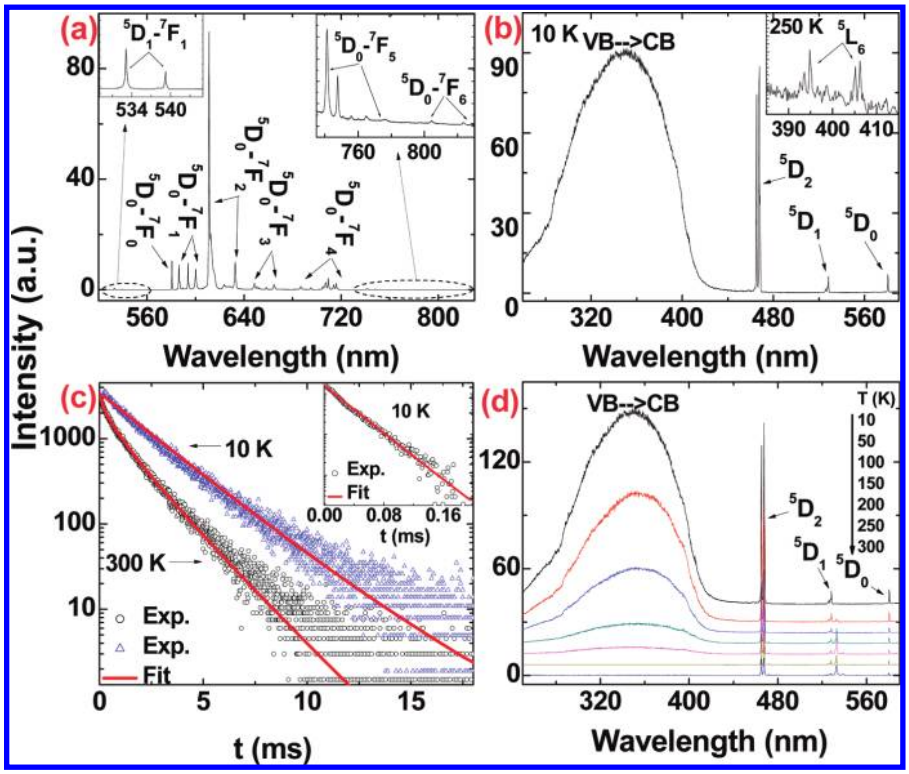


**Figure 2.** Optical spectra and luminescence decays of $Eu^{3+}$ at $C_2$ site in $In_2O_3$ nanocrystals: (a) 10 K emission spectrum upon excitation at 465.1 nm; (b) 10 K excitation spectra by monitoring the $^5D_0 \rightarrow {}^7F_2$ transition at 611.0 nm; the inset shows the 250 K excitation spectrum in the region of $^5L_6$; (c) 10 and 300 K luminescence decays from $^5D_0$ excited at 465.1 nm by monitoring the emission at 611.0 nm; the inset shows the 10 K luminescence decay from $^5D_1$ excited at 465.1 nm by monitoring the $^5D_1 \rightarrow {}^7F_1$ transition at 532.5 nm; (d) 10−300 K excitation spectra by monitoring the emission at 611.0 nm.

excitation peaks from the $^7F_0 \rightarrow {}^5D_1$ transition of $Eu^{3+}(S_6)$ were observed (Figure 3c). Unlike the case of $Gd_2O_3$:$Eu^{3+}$ or $Y_2O_3$:$Eu^{3+}$,[19] ET between the sites of $Eu^{3+}(S_6)$ and $Eu^{3+}(C_2)$ were not observed in the samples. As shown in Figure 3e, the decay curve of the $^5D_0 \rightarrow {}^7F_1$ transition of $Eu^{3+}(S_6)$ measured at 10 K deviates slightly from single exponential in the tail of long time. By fitting with biexponential function, the decay lifetimes are determined to be 13.6 (97.8%) and 16.2 ms (2.2%), respectively. The shorter lifetime component is found very close to that fitted with single exponential (13.8 ms). The very long luminescence lifetime from $^5D_0$ of $Eu^{3+}(S_6)$ is consistent with the fact that the transitions from the $S_6$ site are of MD nature.

**3.3. CF Analysis.** Generally, the CF interaction is relatively weak compared to electrostatic and spin−orbit coupling because the partially filled 4*f* shell is shielded by the filled 5s and 5p orbitals. The commonly used effective operator Hamiltonian is

$$H = H_{\mathrm{FI}} + H_{\mathrm{CF}} \quad (1)$$

where the free ion (FI) Hamiltonian can be expressed as

$$H_{\mathrm{FI}} = E_{\mathrm{avg}} + \sum_{k=2,4,6} F^k f_k + \zeta_f A_{\mathrm{SO}} + \alpha L(L+1) + \beta G(R_2) + \gamma G(R_7) + \sum_{i=2,3,4,6,7,8} T^i t_i + \sum_{h=0,2,4} M^h m_h + \sum_{f=2,4,6} P^f p_f \quad (2)$$

The physical meaning of these FI parameters has been described by Crosswhite and Carnall et al.[20,21] The single-particle CF Hamiltonian is expressed in Wybourne's notation,[22]

$$H_{\mathrm{CF}} = \sum_{k,q} \mathrm{Re}\, B_q^k [C_q^k + (-1)^q \cdot C_{-q}^k] + i\, \mathrm{Im}\, B_q^k [C_q^k - (-1)^q \cdot C_{-q}^k] \quad (3)$$

The number of independent nonvanishing CF parameters is determined by the site symmetry. Due to the low site symmetry, all the independent CF parameters except $B_0^k$ are complex, each having real and imaginary parts denoted by Re $B_q^k$ and Im $B_q^k$, respectively. For $Eu^{3+}$ ion at the $C_2$ site, $kq$ = 20, 22, 40, 42, 44, 60, 62, 64 and 66, with a total number of 15 CF parameters. An axis rotation is introduced to make the imaginary part of $B_2^2$ equal to zero, which reduces the total number of independent CF parameters from 15 to 14.

The energy-level fitting was performed by means of the parametrization of an effective operator Hamiltonian using the *f*-shell empirical programs from Prof. M. F. Reid.[23] Detailed calculation scheme for $Eu^{3+}$ ions at $C_2$ site has been described in $Gd_2O_3$:$Eu^{3+}$.[24] For $In_2O_3$:$Eu^{3+}$ nanocrystals, the FI parameters of $LaF_3$:$Eu^{3+}$[25] and CF parameters of $In_2O_3$:$Eu^{3+}$[12] were used as starting values. First, those most reliable CF levels were fitted by using the truncated $4f^6$ wave functions and freely varying both the five FI parameters ($E_{avg}$,$F^k$, $\zeta_f$) and the 14 CF parameters. The other FI parameters were fixed at the parameters of $LaF_3$:$Eu^{3+}$; second, the above fit was finely tuned by introducing the remaining FI parameters or adding more CF levels of other multiplets such as those congested levels, or both; third, those uncertain CF levels were relocated or reassigned to avoid anomalously large root-mean-square (rms) deviation of

**TABLE 1: Energy Levels of $Eu^{3+}$ at the $C_2$ Site of $In_2O_3$ Nanocrystals**

| multiplet | energy ($cm^{-1}$) exp | energy ($cm^{-1}$) fit | $\Delta E$ ($cm^{-1}$)[a] |
|---|---|---|---|
| $^7F_0$ | 0 | 2 | −2 |
| $^7F_1$ | 173 | 184 | −11 |
| | 389 | 396 | −7 |
| | 566 | 582 | −16 |
| $^7F_2$ | 866 | 852 | 14 |
| | 900 | 879 | 21 |
| | 975 | 961 | 14 |
| | 1191 | 1172 | 19 |
| | 1422 | 1415 | 7 |
| $^7F_3$ | 1797 | 1803 | −6 |
| | 1854 | 1867 | −13 |
| | 1898 | 1908 | −10 |
| | 1961 | 1963 | −2 |
| | 2026 | 2037 | −11 |
| | 2176 | 2178 | −2 |
| | − | 2234 | |
| $^7F_4$ | 2663 | 2665 | −2 |
| | 2812 | 2798 | 14 |
| | 2841 | 2851 | −10 |
| | 3040 | 3039 | 1 |
| | 3085 | 3070 | 15 |
| | 3130 | 3128 | 2 |
| | 3219 | 3216 | 3 |
| | 3260 | 3252 | 8 |
| | 3283 | 3287 | −4 |
| $^7F_5$ | 3742 | 3739 | 3 |
| | 3856 | 3853 | 3 |
| | 3912 | 3903 | 9 |
| | 3933 | 3924 | 9 |
| | 3999 | 3994 | 5 |
| | 4076 | 4078 | −2 |
| | | 4089 | |
| | 4149 | 4157 | −8 |
| | 4337 | 4342 | −5 |
| | 4356 | 4358 | −2 |
| | | 4421 | |
| $^7F_6$ | 4798 | 4812 | −14 |
| | | 4819 | |
| | 5086 | 5104 | −18 |
| | | 5128 | |
| | | 5141 | |
| | 5159 | 5143 | 16 |
| | | 5405 | |
| | | 5412 | |
| | | 5434 | |
| | | 5529 | |
| | | 5533 | |
| | | 5696 | |
| | | 5696 | |
| $^5D_0$ | 17229 | 17229 | 0 |
| $^5D_1$ | 18932 | 18910 | 22 |
| | 18968 | 18964 | 4 |
| | 19020 | 19048 | −28 |
| $^5D_2$ | 21365 | 21372 | −7 |
| | | 21378 | |
| | 21395 | 21392 | 3 |
| | | 21463 | |
| | 21501 | 21490 | 11 |
| | | 24153 | |
| | | 24201 | |
| | | 24227 | |
| | | 24235 | |
| | | 24261 | |
| | | 24282 | |
| | | 24291 | |
| $^5L_6$ | | 24557 | |
| | | 24595 | |
| | | 24618 | |
| | | 24632 | −14 |
| | 24704 | 24697 | 7 |
| | | 24703 | |
| | | 24779 | |
| | | 24829 | |
| | | 25018 | |
| | | 25239 | |
| | | 25310 | |
| | 25329 | 25330 | −1 |
| | 25406 | 25400 | 6 |
| | 25471 | 25466 | 5 |

[a] The energy difference, $\Delta E = E_{exp} - E_{fit}$.

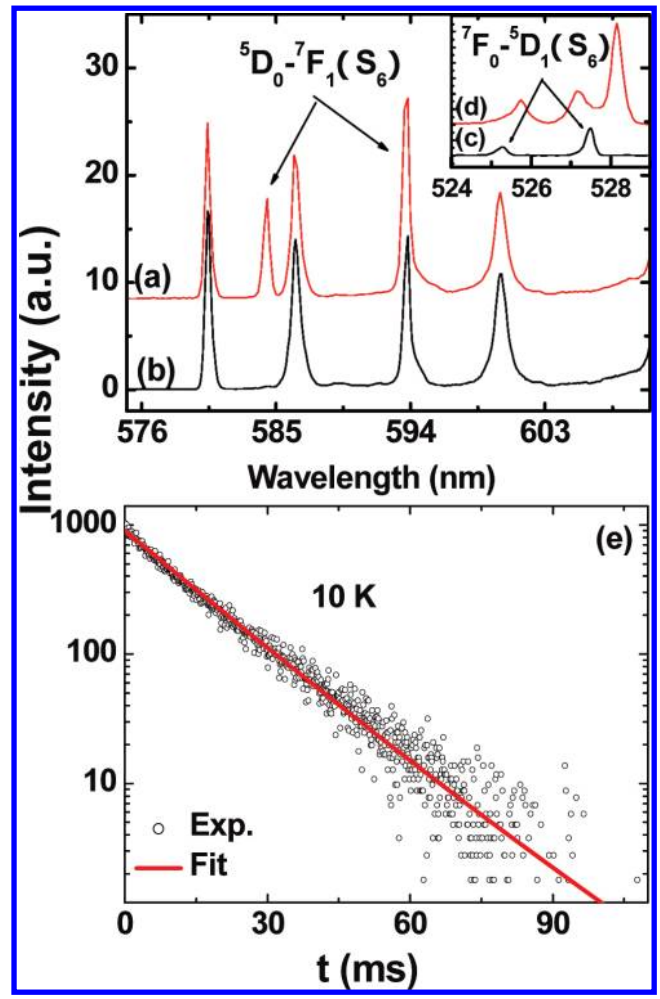


**Figure 3.** 10 K emission spectra upon (a) bandgap excitation at 350 nm, and (b) direct excitation at 465.1 nm of $Eu^{3+}(C_2)$ in $In_2O_3$ nanocrystals. The inset shows the 10 K excitation spectra by monitoring (c) the $^5D_0 \rightarrow {}^7F_1$ ($S_6$) transition at 584.4 nm, and (d) the $^5D_0 \rightarrow {}^7F_2$ ($C_2$) transition at 611.0 nm. (e) 10 K luminescence decay from $^5D_0$ of $Eu^{3+}(S_6)$ by monitoring the emission at 584.4 nm upon excitation at 350 nm.

the fit; and finally the 19 free parameters were simultaneously varied to fit all CF levels we observed without the truncation of the $4f^6$ wave functions. The rms deviation of the final fit is only 13.8 $cm^{-1}$. The fitted energy levels are compared with experimental values in Table 1. The FI and CF parameters are listed in Table 2. The CF parameters of $B_0^2$, Im $B_0^2$, $B_0^6$, Im $B_2^6$, Im $B_4^6$, and Im $B_6^6$ are significantly different from that reported by Antic-Fidancev et al.[12] as compared in Table 2, which is

**TABLE 2: FI and CF Parameters of $Eu^{3+}$ at the $C_2$ Site of $In_2O_3$ Nanocrystals (in $cm^{-1}$)[a]**

| parameter | $C_2$ ($In_2O_3$) | $C_2$ ($In_2O_3$)[b] | $C_2$ ($Y_2O_3$)[c] |
|---|---|---|---|
| $E_{avg}$ | 62791(56) | | |
| $F^2$ | 80206(108) | | 90223 |
| $F^4$ | 59968(774) | | 60257 |
| $F^6$ | 41068(465) | | 44578 |
| $\xi$ | 1313(3) | | 1320 |
| $\alpha$ | 21.4 | | |
| $\beta$ | −567 | | |
| $\gamma$ | 1500 | | |
| $T^2$ | 300 | | |
| $T^3$ | 40 | | |
| $T^4$ | 60 | | |
| $T^6$ | −300 | | |
| $T^7$ | 370 | | |
| $T^8$ | 320 | | |
| $M^0$ | 2.1 | | |
| $P^2$ | 360 | | |
| $B_0^2$ | −168(47) | −54 | −276 |
| $B_2^2$ | −806(27) | −743 | −740 |
| $B_0^4$ | −1206(21) | −1400 | −1385 |
| $ReB_2^4$ | −1951(57) | −1803 | −1431 |
| $ImB_2^4$ | −221(162) | −370 | −509 |
| $ReB_4^4$ | 1133(62) | 1273 | 802 |
| $ImB_4^4$ | −271(243) | 552 | 780 |
| $B_0^6$ | 143(96) | 398 | 304 |
| $ReB_2^6$ | 452(68) | 382 | 159 |
| $ImB_2^6$ | 465(101) | 271 | 198 |
| $ReB_4^6$ | 1124(68) | 959 | 555 |
| $ImB_4^6$ | −313(219) | 442 | 585 |
| $ReB_6^6$ | −30 (90) | −3 | 81 |
| $ImB_6^6$ | −253(93) | 254 | 66 |
| $rms$[d] | 13.8 | 3.9 | 10.3 |

[a] Values in parentheses are errors in the indicated parameters which were freely varied in the fit. The other FI parameters were fixed at the parameters of $LaF_3$:$Eu^{3+}$.[25] [b] Reference 12. [c] Reference 26. [d] The *rms* deviation between the experimental and calculated energies was used as a figure of merit to describe the quality of a fit, with $rms = \sqrt{\sum(E_{exp} - E_{calc})^2/(N - P)}$, where $N = 48$, the number of levels fit, and $P = 19$, the number of parameters freely varied.

most probably due to much less experimental data included in their energy level fitting. In Antic-Fidancev et al.'s analysis, the experimental data were restricted to only 21 CF levels of the $^7F_J$ ($J = 0, 1, 2, 3, 4$) multiplets, thus the reliability of the sixth-rank parameters is lower than that of the second- and fourth-rank parameters. The obtained CF parameter is also compared with that of cubic $Y_2O_3$:$Eu^{3+}$[26] in Table 2. The FI and second-rank CF parameters of fitting results are close to that of $Y_2O_3$:$Eu^{3+}$, but the other CF parameters differ appreciably in magnitude. Particularly, the Im $B_4^4$, Im $B_4^6$, Im $B_6^6$, and Re $B_6^6$ values of $Eu^{3+}$ in $In_2O_3$ have opposite signs, indicating a different CF environment experienced by $Eu^{3+}$ in the $In_2O_3$ host.

The scalar CF strength ($S$) that reflects the overall CF interaction in nanocrystals is calculated to be 790 $cm^{-1}$, according to Chang's definition:[27]

$$S = \left(\frac{1}{3}\sum_{2,4,6}\frac{1}{2k+1}\sum_{q}|B_q^k|^2\right)^{1/2} \quad (4)$$

The CF strengths of $Eu^{3+}$ ions in some common inorganic crystals with different site symmetries are compared in Table 3. The CF strength of $Eu^{3+}$ in $In_2O_3$ host is relatively large, as shown in Table 3, which confirms the low site symmetry of

**TABLE 3: CF Strengths of $Eu^{3+}$ Ions in Different Hosts[a]**

| host | symmetry | $S$ ($cm^{-1}$) |
|---|---|---|
| $LaCl_3$ | $C_{3h}$ | 192 |
| $LaF_3$ | $C_{2v}$ | 346 |
| $KY_3F_{10}$ | $C_{4v}$ | 323 |
| $LiYF_4$ | $S_4$ | 379 |
| $Cs_2NaYCl_6$ | $O_h$ | 498 |
| $YVO_4$ | $D_{2d}$ | 250 |
| $Lu_2O_2S$ | $C_{3v}$ | 395 |
| $LaAlO_3$ | $D_3$ | 440 |
| $Y_3Al_5O_{12}$ | $D_2$ | 682 |
| $Gd_2O_3$ | $C_2$ | 662 |
| $Y_2O_3$ | $C_2$ | 673 |
| $Lu_2O_3$ | $C_2$ | 718 |
| $In_2O_3$ | $C_2$ | 790 |

[a] Data of the CF strengths of $Eu^{3+}$ in the hosts except $In_2O_3$ are from ref 24.

$Eu^{3+}$ in the lattice site of $In_2O_3$. It is revealed that the CF strength of $Eu^{3+}$ decreases with increasing ionic radius of the host cations for the $M_2O_3$ series (M = In, Lu, Y, Gd).[24,28] In general, a lower site symmetry occupied by RE ions in a host gives rise to a larger CF strength.

**3.4. JO Intensity Calculation.** JO intensity parameters, in terms of $\Omega_t$ ($t = 2, 4, 6$), are crucial to evaluating the performance of the laser and luminescent materials.[29,30] The JO intensity parameters $\Omega_{2,4,6}$ of $Eu^{3+}$ at $C_2$ site of $In_2O_3$ nanocrystals can be calculated by a modified method originally proposed by Krupke.[31] This method takes advantage of the fact that the emission intensities of the $^5D_0 \rightarrow {}^7F_2$, $^5D_0 \rightarrow {}^7F_4$, and $^5D_0 \rightarrow {}^7F_6$ transitions are solely dependent on the $\Omega_2$, $\Omega_4$, and $\Omega_6$ parameters, respectively. Different from the method proposed by Krupke, the total transition rate (or lifetime) of $^5D_0$, instead of the calculated MD transition rate of $^5D_0 \rightarrow {}^7F_1$, is used as a standard to determine the absolute values of $\Omega_{2,4,6}$ in this work. The radiative transition rates of $^5D_0 \rightarrow {}^7F_{J'}$ are determined as

$$A_{tot}(J \rightarrow J') = A_{ED}(J \rightarrow J') + A_{MD}(J \rightarrow J') = \beta(J \rightarrow J')\tau_r^{-1} \quad (5)$$

$$\beta(J \rightarrow J') = \frac{\int \lambda I_{J'}(\lambda)\, d\lambda}{\sum_{J'}\int \lambda I_{J'}(\lambda)\, d\lambda} \quad (6)$$

where $\tau_r$ is the radiative lifetime of $^5D_0$, with a value of 455 $s^{-1}$ (see section 3.5), and $I_{J'}(\lambda)$ is the observed luminescence intensity of the $^5D_0 \rightarrow {}^7F_{J'}$ transition. The luminescence branching ratios ($\beta$) of the $^5D_0$ state were experimentally determined by integrating the emission bands in Figure 2a. Once the ED radiative transition rates of $^5D_0 \rightarrow {}^7F_J$ ($J = 2, 4, 6$) are determined, the JO intensity parameters $\Omega_{2,4,6}$ can be calculated using the following formula:

$$A_{ED}(J \rightarrow J') = \frac{64\pi^4 e^2}{3h(2J+1)\bar{\lambda}^3}\frac{n(n^2+2)^2}{9}\sum_{t=2,4,6}\Omega_t|\langle \Phi J \left\| U^{(t)} \right\| \Phi' J'\rangle|^2 \quad (7)$$

where $n$ is the effective index of refraction for the nanocrystals, as will be discussed in section 3.5; $\bar{\lambda}$ is the mean wavelength of the emission band; $|\langle \Phi J \| U^{(t)} \| \Phi' J'\rangle|^2$ represents the reduced

matrix elements (RMEs) of the unit tensor, which were calculated based on the intermediate-coupling wave functions derived from the energy-level fitting. Considering the case of no J-mixing, the three JO intensities $\Omega_{2,4,6}$ are determined to be 14.46, 3.92, and 0.29 (in units of $10^{-20}$ $cm^2$), respectively. As listed in Table S1 (Supporting Information), the $\Omega_{2,4,6}$ parameters obtained are comparable to those values for $Y_2O_3$:$Eu^{3+}$ or $Gd_2O_3$:$Eu^{3+}$ having the same crystal structures. The $\Omega_2$ value of $Eu^{3+}$ in $In_2O_3$ is rather large as compared to those in Table S1, which reflects the hypersensitivity of the $^5D_0 \rightarrow {}^7F_2$ transition and the low site symmetry occupied by $Eu^{3+}$ in the In lattices. The RMEs of the unit tensor of $Eu^{3+}$ in $In_2O_3$ nanocrystals were calculated by using the JJINT program provided by Prof. M. F. Reid.[23] Table S2 compares the values of $U^{(2)}$, $U^{(4)}$, and $U^{(6)}$for $Eu^{3+}$ in different hosts. The RMEs of $In_2O_3$:$Eu^{3+}$ are close to those of $Gd_2O_3$:$Eu^{3+}$ because of similar FI parameters adopted for both hosts. The value of $U^{(6)}$for $Eu^{3+}$ in the form of FI was anomalously larger than that in $In_2O_3$, presumably due to the truncation of the singlet and triplet components from the intermediate-coupling wave functions of $Eu^{3+}$.[32]

**3.5. Luminescence Dynamics.** The luminescence decays of the $^5D_0 \rightarrow {}^7F_2$ transition of $Eu^{3+}(C_2)$ in $In_2O_3$ nanocrystals and submicrometer counterparts have been measured at 10 and 300 K. The decay curves of $Eu^{3+}$ in $In_2O_3$ submicrometer counterparts fit well to a single exponential (Figure S3). The $^5D_0$ lifetime is determined to be 0.81 ms at 300 K and weakly dependent on the temperature. Thus, the observed $^5D_0$ lifetime of $Eu^{3+}$ in $In_2O_3$ submicrometer counterparts can be approximately regarded as the radiative lifetime, considering the large energy gap between $^5D_0$ and its next low-lying $^7F_6$ (12000 $cm^{-1}$). Similar to the case of $Eu^{3+}(S_6)$, the decay from $^5D_0$ of $Eu^{3+}$ in $In_2O_3$ nanocrystals at 10 K slightly deviates from single exponential in the tail upon direct excitation of the $^7F_0 \rightarrow {}^5D_2$ transition at 465.1 nm (Figure 2c). By fitting with biexponential function, the luminescence lifetimes are determined to be 2.21 (96.9%) and 2.64 ms (3.1%), respectively. For comparison, the decay curve is also fitted using a single exponential function, and the lifetime is determined to be 2.23 ms. It can be seen clearly that the shorter lifetime component dominates the whole decay curve, which is generally consistent with that obtained from the single exponential fit. The longer lifetime component observed in the tail may be caused by the smaller $In_2O_3$:$Eu^{3+}$ nanocrystals in our inhomogeneously size-distributed samples, as revealed in $Y_2O_3$:$Eu^{3+}$ nanocrystals previously.[33] In view of their close values obtained from either single- or biexponential fit, hereafter, the intrinsic lifetime for $^5D_0$ of $Eu^{3+}$ $(C_2)$ at 10 K refers to that fitted with single exponential function. As shown in Figure 2c, the decay curve measured at 300 K deviates obviously from single exponential function. Similar nonexponential decay of $Eu^{3+}$ in $In_2O_3$ nanocrystals was also observed at a concentration as low as 0.5 at %, thus the effect of concentration quenching on such decay deviation of $Eu^{3+}$ could be ruled out. Since no photoluminescence (PL) of other sites is observed upon direct excitation of $Eu^{3+}(C_2)$, the nonexponential decay may be caused by a nonradiative ET process from $Eu^{3+}$ ions to the neighboring defects that have close energy levels to the $^5D_0$ state. Such defects might be related to the oxygen vacancies formed in $In_2O_3$ nanocrystals.[34] The decay curve at 300 K fits well to the Inokuti−Hirayama model:[35]$I(t) = I_0 \exp[-t/\tau_0 - C(t/\tau_0)^{1/2}]$, assuming the electric dipole−dipole interaction between donor and acceptor, where $I(t)$ is the time-dependent PL intensity, $I_0$ is the initial intensity, $C$ is a freely varied parameter, $t$ is the time, and $\tau_0$ is the intrinsic luminescence lifetime. The intrinsic lifetime of $^5D_0$ is fitted to be 2.20 ms at 300 K, which is very close to that measured at 10 K (2.23 ms). Vela et al.[15] recently reported a relatively small $^5D_0$ lifetime (less than 0.6 ms) of $Eu^{3+}$ in $In_2O_3$ QDs, which was synthesized via a high temperature injection method that might result in abundant defect states in the $In_2O_3$ host. Thus the remarkable reduction of the $^5D_0$ lifetime of $Eu^{3+}$ in their samples may be caused by the strong nonradiative ET from $Eu^{3+}$ to neighboring defect states. The decay curve of the $^5D_1 \rightarrow {}^7F_1$ emission of $Eu^{3+}(C_2)$ in $In_2O_3$ nanoparticles was measured upon 465.1 nm excitation of the $^7F_0 \rightarrow {}^5D_2$ transition at 10 K, and the $^5D_1$ lifetime is determined to be 27 (97.1%) and 31 $\mu$s (2.9%) fitted with the biexponential function (inset of Figure 2c). The decay time of $^5D_1$ is sensitive to temperature and is reduced significantly with increasing temperature. As a result, the luminescence from $^5D_1$ vanished at 300 K.

The $^5D_0$ lifetime of $Eu^{3+}(C_2)$ in $In_2O_3$ nanocrystals is much longer than that of its submicrometer counterparts. There are many factors that may influence the $^5D_0$ radiative lifetime of $Eu^{3+}$ in nanocrystals such as the nonsolid media[33] and the changes of lattice constants.[36] As shown in the following, the nonsolid medium surrounding the $In_2O_3$:$Eu^{3+}$ nanoparticles with different effective indices of refraction ($n_{eff}$) affects the $^5D_0$ lifetime of $Eu^{3+}$ most significantly. The radiative lifetime can be expressed as

$$\tau_r^{-1} = \frac{64\pi^4 e^2}{3h(2J+1)\bar{\lambda}^3}[\chi_{ED} \sum_{t=2,4,6} \Omega_t |\langle \Phi J \| U^{(t)} \| \Phi' J' \rangle|^2 + \chi_{MD} |\langle \Phi J \| M \| \Phi' J' \rangle|^2] \quad (8)$$

where $M$ is the MD moment for transition from $J$ to $J'$, and $\chi_{ED}$ and $\chi_{MD}$ are the correction factors of the refractive index ($n$) for ED and MD transitions, respectively, with $\chi_{ED} = n(n^2 + 2)^2/9$ and $\chi_{MD} = n^3$. The wavelength-dependent refractive index, $n$, of cubic $In_2O_3$ was derived from the Cauchy formula[37]$n(\lambda$,unit: nm$) = 1.81 + 2.1 \times 10^4/\lambda^2$. For $In_2O_3$ nanocrystals, the effective index of refraction ($n_{eff}$) can be expressed as $n_{eff} = n(\lambda)_{In2O3} \cdot x + (1 - x) \cdot n_{med}$, where $n(\lambda)_{In2O3}$is the refractive index of $In_2O_3$ (1.866 at the wavelength of 611 nm), $x$ is the filling factor showing what fraction of space is occupied by nanocrystals with the refractive index of $n(\lambda)_{In2O3}$, and $n(\lambda)_{med}$ is the refractive index of the medium.[33] We have measured the $^5D_0$ lifetimes of $Eu^{3+}(C_2)$ in $In_2O_3$ nanocrystals immersed in solvents with different refractive indices at 300 K. The solvents included methanol ($CH_3OH$, $n = 1.329$), ethanol ($C_2H_5OH$, $n = 1.361$), n-hexanol ($CH_3(CH_2)_4CH_2OH$, $n = 1.418$), carbon tetrachloride ($CCl_4$, $n = 1.460$) and toluene ($C_6H_5CH_3$, $n = 1.497$). The decay curves were all well fitted by the Inokuti−Hirayama model mentioned above. Figure 4 presents the dependence of the intrinsic radiative lifetime of $^5D_0$ on the refractive index of medium ($n_{med}$) for $Eu^{3+}(C_2)$ ions in $In_2O_3$ nanocrystals. Apparently, the $^5D_0$ lifetime is significantly affected by the surrounding medium. The larger refractive index of the surrounding medium results in the smaller radiative lifetime of $^5D_0$. The experimental $^5D_0$ lifetimes for various media were fitted to eq 8, using $x$ as a variable parameter. The filling factor was determined to be 0.43. Thus, it is clearly shown that the longer $^5D_0$ lifetime of $Eu^{3+}$ in $In_2O_3$ nanocrystals than in submicrometer counterparts is mainly due to the change of the refractive index of the nonsolid surrounding medium.

**3.6. Host-to-$Eu^{3+}$ ET.** The $Eu^{3+}$ luminescence sensitized by $In_2O_3$ nanoparticles has attracted much attention for various material applications.[14–16,38–40] The broad band centered at 350

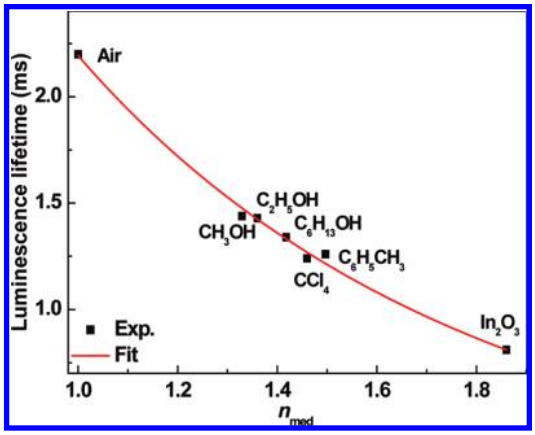


**Figure 4.** Dependence of the $^5D_0$ lifetimes of $Eu^{3+}(C_2)$ in $In_2O_3$ nanocrystals on the refractive index of the surrounding medium at 300 K.

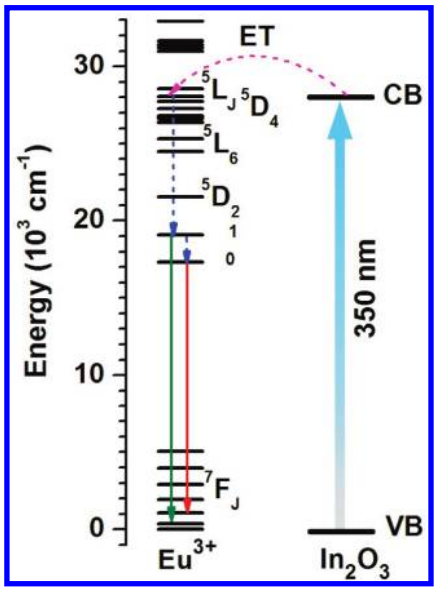


**Figure 5.** An ET mechanism describing the sensitization of $In_2O_3$ nanocrystals to $Eu^{3+}$ ions. The dotted, straight, and dashed arrows denote multiphonon nonradiative transitions, radiative transitions, and ET processes, respectively.

nm in the excitation spectra as well as the intense $Eu^{3+}$ emissions upon bandgap excitation indicate an efficient ET from the $In_2O_3$ host to $Eu^{3+}$ ions. Previously, effective ET processes from $In_2O_3$ nanoparticles to $Eu^{3+}$ embedded in the $SiO_2$ matrix were observed, which were argued to transfer via the $O^{2-}-Eu^{3+}$ charge transfer band[38] or defect states[39] instead of the direct transfer to the RE energy levels. Here, based on the optical properties of $In_2O_3$:$Eu^{3+}$ nanocrystals we observed at temperatures between 10 and 300 K, a possible ET mechanism from $In_2O_3$ host to $Eu^{3+}$ is proposed. As schematically plotted in Figure 5, the bandgap energy of $In_2O_3$:$Eu^{3+}$ nanocrystals is close to the energy levels of $^5L_J$ or $^5D_4$ of $Eu^{3+}$ ions, which may facilitate the nonradiative ET from the $In_2O_3$ host to $Eu^{3+}$ ions. Upon excitation above the bandgap, an electron−hole pair (carrier) is formed in the $In_2O_3$ host. The recombination of electron−hole pair will resonantly transfer its energy to the $^5L_J$ or $^5D_4$ state of $Eu^{3+}$, followed by nonradiative relaxation to $^5D_1$ and $^5D_0$ states of $Eu^{3+}$, and then the characteristic red luminescence of $Eu^{3+}$ is observed. Such ET mechanism is also applicable for $In_2O_3$:$Eu^{3+}$ submicrometer counterparts, where the electron−hole pair may nonradiatively transfer its energy to $Eu^{3+}$ via the lower CF levels of $^5L_J$ or $^5D_4$.

To further probe the host-to-$Eu^{3+}$ ET efficiency, the excitation spectra of $In_2O_3$:$Eu^{3+}$ nanocrystals were measured at various temperatures. As shown in Figure 2d, the intensity of the broad excitation band centered at 350 nm drastically decreases with the increase of temperature and is completely quenched at 250 K, which indicates the decrease of ET efficiency as the temperature increases. There are two main factors that may result in the observed thermal quenching: (1) nonradiative ET from the excited state of $RE^{3+}$ ions to semiconductor bandgap or defect states, which is characterized by a remarkable decrease of $RE^{3+}$ lifetime;[41−43] (2) nonradiative recombinations of electron−hole pairs near defects in the semiconductor host prior to their transfer to $RE^{3+}$.[44,45] As has been discussed in section 3.5, the $^5D_0$ lifetime of $Eu^{3+}$ changes little at 10−300 K for $In_2O_3$:$Eu^{3+}$ nanocrystals, thus the possibility of strong nonradiative ET from $Eu^{3+}$ to $In_2O_3$ bandgap states or defects is excluded. Such thermal quenching of the excitation band at 250 K is very likely ascribed to nonradiative recombination of electron−hole pairs in $In_2O_3$ host, which may involve deep traps (such as oxygen vacancies) and Auger processes in $In_2O_3$. Interestingly, the quenching temperature of the broad excitation band in $In_2O_3$:$Eu^{3+}$ nanocrystals is much higher than that of submicrometer counterparts (quenched at 150 K, Figure S1), indicating less sensitive temperature dependence of the host-to-$Eu^{3+}$ ET in $In_2O_3$:$Eu^{3+}$ nanocrystals. This high quenching temperature in $In_2O_3$:$Eu^{3+}$ nanocrystals is presumably due to the effective restraint of ET from $RE^{3+}$ to the surface defects, which may be caused by the existence of much more grain boundaries in $In_2O_3$:$Eu^{3+}$ nanocrystals compared to that of its submicrometer counterparts. Likewise, such high thermal quenching temperature was also observed in $LaPO_4$:$Eu^{3+}$ and $Y_2O_3$:$Tb^{3+}$ nanostructures.[46,47]

## 4. Conclusions

The optical spectroscopy and luminescence dynamics of $Eu^{3+}$ in $In_2O_3$ nanocrystals, which were synthesized via a simple solvothermal method, have been systematically investigated at temperatures between 10 and 300 K. Forty-eight CF levels below 25500 cm$^{-1}$ of $Eu^{3+}$ at the $C_2$ site of $In_2O_3$ have been experimentally determined for the first time. By means of the parametrization of an effective operator Hamiltonian including 19 freely varied FI and CF parameters, energy-level fitting yields a small standard deviation (13.8 cm$^{-1}$) from the experiments. It is revealed that the CF strength of Eu at the $C_2$ site is as large as 790 cm$^{-1}$. Different from that of $Gd_2O_3$:$Eu^{3+}$ or $Y_2O_3$:$Eu^{3+}$, ET between the $Eu^{3+}$ sites of $S_6$ and $C_2$ does not occur. On the basis of a modified JO calculation method for $Eu^{3+}$, the JO intensity parameters $\Omega_{2,4,6}$ have been determined to be 14.46, 3.92, and 0.29 (in units of $10^{-20}$ cm$^2$), indicative of the good performance of nanophosphors. The luminescence lifetimes of $^5D_0$ of $Eu^{3+}(C_2)$ in $In_2O_3$ nanocrystals were measured to be 2.23 ms, which is about three times longer than that in submicrometer or bulk counterparts. It has been validated that the $^5D_0$ lifetime of $Eu^{3+}(C_2)$ depends critically on the surrounding medium of nanocrystals that have a filling factor of 0.43. Furthermore, as compared to the submicrometer counterparts, an enhanced host-to-$Eu^{3+}$ ET with higher quenching temperature has been demonstrated in $In_2O_3$:$Eu^{3+}$ nanocrystals due possibly to photon-induced carrier localization and trapping around $Eu^{3+}$. The comprehensive study of electronic structure and optical properties of $Eu^{3+}$ in such novel nanophosphors are of great importance to material applications such as the fabrication of electroluminescence devices and luminescent nanobiolabels.

**Acknowledgment.** This work is supported by the Hundreds of Talents Program of the Chinese Academy of Sciences (CAS), Knowledge Innovation Program of CAS for Key Topics (No. KJCX2-YW-358), the NSFC (Nos. 10774143 and 10974200), the 973 and 863 programs of MOST (Nos. 2007CB936703 and 2009AA03Z430), Fujian Provincial Science Fund for Distinguished Young Scholars (No. 2009J06030), and the Key Project of Science and Technology Foundation of Fujian Province (No. 2007I0024).

**Supporting Information Available:** The excitation spectra of $Eu^{3+}$ ions in $In_2O_3$ submicrometer counterparts; plot of $F(R)^2$ versus photon energy for direct transition of $In_2O_3$:$Eu^{3+}$ nanocrystals annealed at different temperatures; luminescence decays from $^5D_0$ of $Eu^{3+}(C_2)$ in $In_2O_3$ submicrometer counterparts at 10 and 300 K; JO intensity parameters of $Eu^{3+}$ ions in different hosts; RMEs of the unit tensor for $Eu^{3+}$ ions in different hosts. This material is available free of charge via the Internet at http://pubs.acs.org.

## References and Notes

(1) Wang, Z. L.; Quan, Z. W.; Jia, P. Y.; Lin, C. K.; Luo, Y.; Chen, Y.; Fang, J.; Zhou, W.; O'Connor, C. J.; Lin, J. *Chem. Mater.* **2006**, *18*, 2030.
(2) Chen, W.; Zhang, J. Z.; Joly, A. G. *J. Nanosci. Nanotechnol.* **2004**, *4*, 919.
(3) Carlos, L. D.; Ferreira, R. A. S.; Bermudez, V. D.; Ribeiro, S. J. L. *Adv. Mater.* **2009**, *21*, 509.
(4) Zeng, J. H.; Su, J.; Li, Z. H.; Yan, R. X.; Li, Y. D. *Adv. Mater.* **2005**, *17*, 2119.
(5) Wang, F.; Liu, X. G. *Chem. Soc. Rev.* **2009**, *38*, 976.
(6) Wang, X.; Kong, X. G.; Yu, Y.; Sun, Y. J.; Zhang, H. *J. Phys. Chem. C* **2007**, *111*, 15119.
(7) Tanner, P. A.; Yu, L. *J. Nanosci. Nanotechnol.* **2008**, *8*, 1307.
(8) Walsh, A.; Da Silva, J. L. F.; Wei, S. H.; Korber, C.; Klein, A.; Piper, L. F. J.; DeMasi, A.; Smith, K. E.; Panaccione, G.; Torelli, P.; Payne, D. J.; Bourlange, A.; Egdell, R. G. *Phys. Rev. Lett.* **2008**, *100*, 167402.
(9) Fuchs, F.; Bechstedt, F. *Phys. Rev. B* **2008**, *77*, 10.
(10) Bourlange, A.; Payne, D. J.; Egdell, R. G.; Foord, J. S.; Edwards, P. P.; Jones, M. O.; Schertel, A.; Dobson, P. J.; Hutchison, J. L. *Appl. Phys. Lett.* **2008**, *92*, 092117.
(11) Liang, C. H.; Meng, G. W.; Lei, Y.; Phillipp, F.; Zhang, L. D. *Adv. Mater.* **2001**, *13*, 1330.
(12) Anticfidancev, E.; Aride, J.; Lemaitreblaise, M.; Porcher, P.; Taibi, M. *J. Alloys Compd.* **1992**, *188*, 242.
(13) Kim, H. K.; Li, C. C.; Barrios, P. J. *J. Vac. Sci. Technol. A* **1994**, *12*, 3152.
(14) Dutta, D. P.; Sudarsan, V.; Srinivasu, P.; Vinu, A.; Tyagi, A. K. *J. Phys. Chem. C* **2008**, *112*, 6781.
(15) Vela, J.; Prall, B. S.; Rastogi, P.; Werder, D. J.; Casson, J. L.; Williams, D. J.; Klimov, V. I.; Hollingsworth, J. A. *J. Phys. Chem. C* **2008**, *112*, 20246.
(16) Choi, Y. G.; Yu, S. M.; Chung, W. *J. Chem. Phys. Lett.* **2008**, *461*, 290.
(17) Xu, J. Q.; Wang, X. H.; Wang, G. Q.; Han, J. J.; Sun, Y. A. *Electrochem. Solid-State Lett.* **2006**, *9*, H103.
(18) Sheng, K. C.; Korenowski, G. M. *J. Phys. Chem.* **1988**, *92*, 50.
(19) Buijs, M.; Meyerink, A.; Blasse, G. *J. Lumin.* **1987**, *37*, 9.
(20) Carnall, W. T.; Goodman, G. L.; Rajnak, K.; Rana, R. S. *J. Chem. Phys.* **1989**, *90*, 3443.
(21) Crosswhite, H. M.; Crosswhite, H. *J. Opt. Soc. Am. B* **1984**, *1*, 246.
(22) Wybourne, B. G. *Spectroscopic Properties of Rare Earths*; Interscience: New York, 1965.
(23) Reid, M. F. f-Shell empirical programs and examples. Private communication.
(24) Liu, L. Q.; Chen, X. Y. *Nanotechnology* **2007**, *18*, 255704.
(25) Carnall, W. T.; Goodman, G. L.; Rajnak, K.; Rana, R. S. A systematic analysis of the spectra of the lanthanides doped into single crystal LaF3. *Argonne National Laboratory Report No. ANL-88−8*, Argonne, Illinois, **1988**.
(26) Faucher, M. D.; Dexpert-Ghys, J. *Phys. Rev. B* **1981**, *24*, 3138.
(27) Chang, N. C.; Gruber, J. B.; Leavitt, R. P.; Morrison, C. A. *J. Chem. Phys.* **1982**, *76*, 3877.
(28) Antic-Fidancev, E.; Holsa, J.; Lastusaari, M. *J. Alloys Compd.* **2002**, *341*, 82.
(29) Ofelt, G. S. *J. Chem. Phys.* **1962**, *37*, 511.
(30) Judd, B. R. *Phys. Rev.* **1962**, *127*, 750.
(31) Krupke, W. F. *Phys. Rev.* **1966**, *145*, 325.
(32) Weber, M. J. *Phys. Rev.* **1968**, *171*, 283.
(33) Meltzer, R. S.; Feofilov, S. P.; Tissue, B.; Yuan, H. B. *Phys. Rev. B* **1999**, *60*, R14012.
(34) Zheng, M. J.; Zhang, L. D.; Li, G. H.; Zhang, X. Y.; Wang, X. F. *Appl. Phys. Lett.* **2001**, *79*, 839.
(35) Inokuti, M.; Hirayama, F. *J. Chem. Phys.* **1965**, *43*, 1978.
(36) Schmechel, R.; Kennedy, M.; von Seggern, H.; Winkler, H.; Kolbe, M.; Fischer, R. A.; Li, X. M.; Benker, A.; Winterer, M.; Hahn, H. *J. Appl. Phys.* **2001**, *89*, 1679.
(37) Prathap, P.; Subbaiah, Y. P. V.; Devika, M.; Reddy, K. T. R. *Mater. Chem. Phys.* **2006**, *100*, 375.
(38) Wan, N.; Xu, J.; Lin, T.; Zhang, X. G.; Xu, L. *Appl. Phys. Lett.* **2008**, *92*, 201109.
(39) Yu, Y. l.; Chen, D. q.; Wang, Y. s.; Huang, P.; Weng, F. y.; Niu, M. t. *Phys. Chem. Chem. Phys.* **2009**, *11*, 8774.
(40) Kudrawiec, R.; Podhorodecki, A.; Mirowska, N.; Misiewicz, J.; Molchan, I.; Gaponenko, N. V.; Lutich, A. A.; Gaponenko, S. V. *Mater. Sci. Eng., B* **2003**, *105*, 53.
(41) Palm, J.; Gan, F.; Zheng, B.; Michel, J.; Kimerling, L. C. *Phys. Rev. B* **1996**, *54*, 17603.
(42) Kik, P. G.; deDood, M. J. A.; Kikoin, K.; Polman, A. *Appl. Phys. Lett.* **1997**, *70*, 1721.
(43) Coffa, S.; Franzo, G.; Priolo, F.; Polman, A.; Serna, R. *Phys. Rev. B* **1994**, *49*, 16313.
(44) Morishima, S.; Maruyama, T.; Akimoto, K. *J. Cryst. Growth* **2000**, *209*, 378.
(45) Nyein, E. E.; Hommerich, U.; Heikenfeld, J.; Lee, D. S.; Steckl, A. J.; Zavada, J. M. *Appl. Phys. Lett.* **2003**, *82*, 1655.
(46) Yu, L. X.; Song, H. W.; Lu, S. Z.; Liu, Z. X.; Yang, L. M.; Wang, T.; Kong, X. G. *Mater. Res. Bull.* **2004**, *39*, 2083.
(47) Song, H. W.; Wang, J. W. *J. Lumin.* **2006**, *118*, 220.

JP102592Q